
# The Role of Native Binder in Controlling the Polytetrafluoroethylene Distribution in Gas Diffusion Layers for Proton Exchange Membrane Fuel

*Fuel Cells*

Fuel Cells
From Fundamentals to Systems

RESEARCH ARTICLE OPEN ACCESS

# The Role of Native Binder in Controlling the Polytetrafluoroethylene Distribution in Gas Diffusion Layers for Proton Exchange Membrane Fuel Cells

Dylan Schulz[1] | Marcus Ringström[2] | Siva Ravi Sankar[1] | Anna Martinelli[1]

[1]Department of Chemistry and Chemical Engineering, Chalmers University of Technology, Gothenburg, Sweden | [2]Department of Applied Electrochemistry, Royal Institute of Technology, Stockholm, Sweden

**Correspondence:** Anna Martinelli (anna.martinelli@chalmers.se)

**Received:** 17 February 2026 | **Revised:** 30 June 2026 | **Accepted:** 7 July 2026

**Keywords:** GDL | identical location Raman/EDX mapping | limiting current density | PEM fuel cells | PTFE distribution

## ABSTRACT

Gas diffusion layers (GDLs), a critical component in $H_2/O_2$ proton exchange membrane fuel cells (PEMFCs), are commonly treated with polytetrafluoroethylene (PTFE) for controlling hydrophobicity. However, the influence of the GDL's native microstructure on the final PTFE spatial distribution is still poorly understood. We compare the PTFE distribution in a dry-laid GDL containing a native binder with that in a wet-laid, binder-free GDL. To analyze the GDL microstructure, we perform scanning electron microscopy (SEM), energy-dispersive X-ray spectroscopy (EDX), and confocal Raman spectroscopy, with $\mu$m resolution at identical locations. We find that the binder acts as a scaffold for PTFE agglomerates to deposit, independent of the fiber locations. We show that PTFE deposited on the binder phase results in a significantly lower effect on the dry oxygen transport resistance, measured using a limiting current method at low oxygen concentration.

## 1 | Introduction

Renewably sourced hydrogen is a key component toward a climate-neutral energy economy [1], while economic analyses suggest that clean hydrogen could meet 24% of the global energy demand already by 2050 [2]. Alongside electrolyzers, fuel cells such as proton exchange membrane fuel cells (PEMFCs) are expected to play a crucial part of this energy economy because of their high volumetric power density, particularly important for transport applications [1]. PEMFCs are, however, constrained by high component and manufacturing costs as well as by challenges related to durability and performance optimization. In particular, water management is a crucial factor that influences the performance of PEMFCs. During operation, water is formed at the cathode catalyst layer (CCL) as a product of the oxygen reduction reaction (ORR), contributing to ionomer hydration and facilitating back-diffusion to the anode. However, some of the water produced during operation may accumulate within the pore space of the gas diffusion layer (GDL), reducing the overall fuel cell efficiency [3].

GDLs are typically made from a source of poly(acrylonitrile) (PAN), which is then carbonized in a nitrogen atmosphere at 1200°C–1350°C to form carbon fibers [3]. From this material, a GDL is made by either applying a binder material to hold the fibers together, as is the case for SGL-39AA (Sigracet) GDLs, or by forming a felt via hydroentangling the carbon fibers, as is the case for Freudenberg F-H23 GDLs. The former process, which uses binders to hold together the carbon fibers, is termed a dry-laid method, whereas the latter hydroentangling process is known as a wet-laid process. The GDL can then be impregnated with PTFE to increase its hydrophobicity [3]. The spatial distribution of PTFE within the GDL porous matrix is inherently discontinuous, and this uneven distribution creates regions with varying hydropho-

bicity and hydrophilicity. In turn, this leads to a mixed wettability situation, characterized by a stochastic distribution of contact angles within the porous matrix. This may result in adverse effects such as inadequate water drainage and local flooding, while other areas may retain less water. This imbalance can severely affect mass transport due to reduced oxygen availability at the CCL [4, 5].

It is clear that the treatment of GDLs with PTFE, along with the microstructure and distribution of PTFE within the GDL, is critical to PEMFC performance [6, 7], wherefore significant research has been done to understand the impact and mechanisms of the PTFE structure and loading on water management. For instance, Mortazavi et al. [8] have studied the dynamic behavior of droplet detachment at the GDL surface for various PTFE loadings, showing that droplets detached at smaller diameters with increasing PTFE loadings due to increased hydrophobicity. Park et al. [9] studied the influence of PTFE on water transport in an active cell, hypothesizing that higher PTFE loadings induce capillary condensation effects that hinder liquid water removal. Fishman and Bazylak [10] used computer tomography (CT) to study the through-plane distribution of PTFE on Toray GDL samples, while Hiroshi Ito et al. [11] used EDX mapping to obtain similar results, and studied the effect on through-plane gas permeability. They also linked differences in the PTFE distribution of their GDLs to the applied drying conditions. Sadeghifar et al. [12] measured the through-plane thermal conductivity under compression for a wide range of (Sigracet) GDL microstructures with different PTFE loadings, showing that PTFE increased the thermal resistance within the GDL structure. This was mainly attributed to the low thermal conductivity of PTFE compared to the carbon-based solid components within the porous structure. Fluckiger et al. [4] used electrochemical diffusimetry to quantify the effects of PTFE on the effective diffusivity for uncoated SGL and Toray GDLs under compression, showing that increasing PTFE loading reduces the effective porosity and increases tortuosity. This was attributed to the reduction of through-plane pore connectivity for increasing PTFE loadings. It was also noted that PTFE deposited significantly on the porous binder, though their work did not focus on mapping this effect.

EDX and Raman have both shown promise in understanding the spatial distribution and structure of PTFE across the GDL. Mendoza et al. [13] used Raman spectroscopy to spatially resolve the chemical information on the carbon and PTFE distribution over GDL surfaces at various PTFE loadings, finding that the peak intensity of PTFE increased monotonically with increasing PTFE loading. Unsintered GDLs showed spots of increased PTFE Raman intensities compared to similar, sintered GDLs demonstrating the need for heat treatment. However, their mapping results focused on large pixel sizes exceeding 10 $\mu$m, limiting information about the micrometer-scale structure. Rofaiel et al. [14] presented a novel approach to quantify the heterogeneous distribution of PTFE over GDL cross sections by combining scanning electron microscopy (SEM) with energy dispersive X-ray spectroscopy (EDX) for various commercially available carbon paper, felt, and cloth GDLs. They showed that carbon paper and felt materials exhibit a highly heterogeneous PTFE distribution across the GDL thickness, with high PTFE concentration at the GDL surface and low concentrations in the GDL interior, porous structure and a high degree of agglomeration rather than a uniform PTFE distribution. However, their work again focused on large areas and did not use GDLs with preexisting binders, thus offering limited information on the $\mu$m-scale structure of PTFE near fibers or other binder structures. Zhuo et al. [15] studied the effect of different PTFE loadings for the GDL in the unified regenerative fuel cell (URFC) context, ultimately recommending a loading with ~21 wt% PTFE for the case of dual fuel cell/electrolyzer use. Kakaee et al. [16], showed that binder structures slow the rate of water evaporation in a GDL. Such structures may then require additional PTFE to combat this trend; hence, understanding the effect that additional PTFE has on fuel cell performance is crucial.

In this work, we examine two different commercial GDLs that we treat with PTFE via dip coating and sintering, as shown in Figure 1. We use both confocal Raman spectroscopy and EDX to chemically map, at identical locations, the planar PTFE distribution for GDLs with and without a preexisting binder. We additionally analyze the cross section of a single GDL without preexisting binder using Raman and EDX, to understand the through-plane PTFE distribution resulting from the employed dipping/sintering method. Confocal Raman spectroscopy enables the distinction between functional groups, such as the C-F bond in PTFE, through characteristic vibrational modes. Collecting spectra point by point in a grid over a selected area allows the presence of PTFE to be spatially mapped by comparing the intensity of the C-F bond response from each collection point, hence yielding a visual map of the PTFE distribution over the analyzed area. EDX functions by analyzing the *X*-ray response of photon de-excitations in a sample after elements in a sample are excited by a focused electron beam. The energy of the resulting *X*-ray photons, 0.677 keV in the case of fluorine, is a distinct fingerprint for the underlying element. As fluorine is only present in the GDL samples as part of the PTFE polymer, it can be used to map PTFE over the analyzed sample area. Finally, to help understand the effect of the applied PTFE treatment on gas transport in operating fuel cells, we have performed limiting current density measurements comparing GDLs of each type with 5 wt% and 20 wt% PTFE loading. These values were determined by analyzing the contact angle of the bulk GDL papers with different PTFE loadings.

This work provides new knowledge on how experimental methods can be integrated for a better understanding of the porous fiber/polymer microstructure in GDL materials. It also provides a direct comparison between the structure of PTFE in GDLs with and without a preexisting binder phase and links these structural characteristics to GDL performance in operating fuel cells, thus offering a valuable pathway to modify and further optimize the GDL microstructure for more efficient PEMFC applications.

## 2 | Materials and Methods

### 2.1 | Hydrophobic Treatment of GDLs

The uncompressed thickness of the GDLs before treatment was measured at 0.025 MPa as 226 ± 5 $\mu$m for the binder-free F-H23 GDL, which lacks a preexisting binder, and 272 ± 6 $\mu$m for the binder-containing SGL-39AA GDL, using a Zwick/Roell Z010

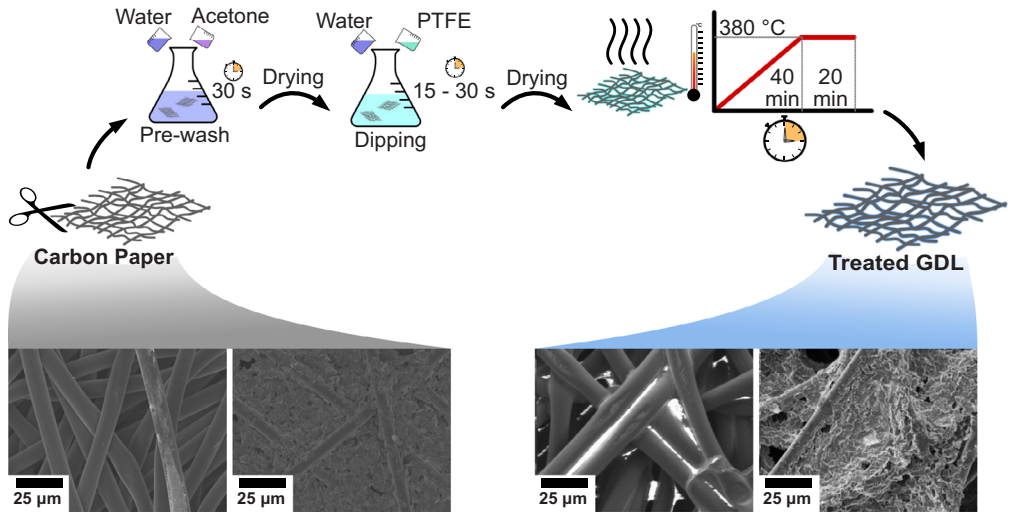


**FIGURE 1** | Schematic representation of the hydrophobization process of the GDL using PTFE dispersion, alongside SEM images of the untreated GDLs (left) and treated GDLs (right). In each pair of SEM images, the first image shows the F-H23 GDL, which lacks a preexisting binder, and the second image shows the SGL-39AA GDL, which contains a preexisting binder.

compression fixture equipped with three inductive thickness sensors. Both GDL materials were purchased from Fuel Cell Store. Before hydrophobic treatment, the GDLs were cut, cleaned, and dried as follows. The GDLs were first cut into uniform pieces for consistent treatment and analysis. The GDL pieces were washed in a 1:1 acetone:water solution and then gently agitated to remove any dust, debris, or other contaminants. After washing, the GDLs were dried for 10 min on absorbent paper and then placed in a calcination oven at 100°C for 1 h to remove any remaining moisture. The dried GDLs were then cooled to room temperature before dipping in the PTFE dispersion.

This hydrophobic treatment, also shown in Figure 1, was inspired by similar procedures found in literature [14, 15, 17] and was performed by immersing the GDL substrates in PTFE dispersions prepared from a 60 wt% PTFE solution. This solution, purchased from Sigma Aldrich, consists of PTFE particles of 200 to 500 nm in diameter dispersed in a mixture of water and tergitol, which we further diluted using MilliQ water to reach the required concentration (see Table 1). The immersion time was 30 s when targeting a 5 wt% PTFE loading, while to target 20 wt% and 50 wt% of PTFE it was necessary, due to the higher PTFE concentrations involved, to reduce the immersion time to 15 s to prevent excessive PTFE deposition and clogging of the pores in the GDL structure. After immersion, the PTFE-coated GDLs were dried on absorbent paper at room temperature for 1 h. This allowed PTFE particles to loosely adhere to the GDL surface before the heat treatment. The GDLs were heat-treated in an oven by first ramping up from room temperature to 380°C over about 40 min and then staying at 380°C for 20 min. This temperature was determined from a thermogravimetric analysis (TGA) performed using a Mettler Toledo Star System combined TGA/DSC 3+ instrument, scanning the temperature range from 30°C to 450°C in nitrogen atmosphere (see Figure S1 in the Supporting Information). This temperature range ensured the removal of the tergitol emulsifier present in the dispersion as well as optimal sintering of PTFE particles onto the GDL surface. Notably, PTFE is reported to be thermally stable up to 400°C [18]. The GDLs were then gradually cooled to room temperature, over 30 min. For clarity, this whole procedure is also schematically illustrated in Figure 1. The amount of PTFE actually taken up by the GDL was measured from the difference in mass before and after the hydrophobic treatment, and is reported in Table 1.[1]

**TABLE 1** | Details of the hydrophobic treatment including PTFE concentration in the dispersion and achieved PTFE loadings after sintering, for the two types of GDL.

| GDL | Concentration in dispersion | Actual wt% of PTFE (average ± std) |
|---|---|---|
| F-H23 | 5 wt% | 7.25 ± 0.15 |
| | 20 wt% | 20.67 ± 0.88 |
| | 50 wt% | 48.46 ± 1.66 |
| SGL-39AA | 5 wt% | 5.04 ± 0.03 |
| | 20 wt% | 19.53 ± 1.17 |
| | 50 wt% | 56.53 ± 0.92 |

## 2.2 | Raman Spectroscopy

Raman spectra were recorded at room temperature and at ambient conditions, fixing the material to be investigated on to a *xyz* motorized stage. The Raman spectra were recorded using an InVia Reflex spectrometer from Renishaw. A near infrared diode laser, with a wavelength of 785 nm and a nominal maximum power of 300 mW, was used as the excitation source. However, to avoid sample damage, the laser power at the sample was limited to 1.5 mW. The diffraction grating had 1200 l/mm, giving a spectral resolution better than 2 $cm^{-1}$. Single spot spectra were obtained by averaging over 10 scans with an exposure time of 20 s each. For in-plane Raman mapping (Figures 3–6), a 50×

Leica objective ($NA$ = 0.50) was used and a 2D rectangular matrix was defined with distinct collection points set 2 $\mu$m apart. For cross-sectional Raman mapping (Figure 7), the GDL was prepared by cryo-cutting in liquid nitrogen. A 20× Leica objective ($NA$ = 0.40) was used, and spectra were collected at spots set 5 $\mu$m apart.

## 2.3 | SEM/EDX

SEM was used to obtain higher resolution images of the GDLs than is possible using a conventional, confocal microscope. The very low numerical aperture of the SEM also allows better imaging across different depths in the porous GDL structure. In addition, EDX spectroscopy was used for elemental mapping using an e-beam acceleration of 5 kV. Carbon ($K_\alpha$ = 0.227 keV) is mainly represented in the GDL fibers and preexisting binder, while fluorine ($K_\alpha$ = 0.677 keV) is exclusively present in the PTFE added during the hydrophobic treatment; both have very characteristic EDX signatures (Figure S2), which enables mapping these elements to complement and verify results achieved from mapping by confocal Raman spectroscopy. A JEOL JSM-7800F Prime SEM equipped with an Oxford Instruments X-MaxN 50 EDX System, made available by the Chalmers Materials Analysis Laboratory (CMAL), was used to acquire SEM and EDX images. A Hitachi TM4000 tabletop SEM with an AztecOne XploreCompact 65 mm$^2$ EDX system, made available by Spectral AB, was used for some further results shown in the Supporting Information.

## 2.4 | Contact Angle

Contact angle measurements (Figure 2) were performed at room temperature using a goniometer from Attension Theta by Biolin Scientific (Finland). Water droplets of 3–5 $\mu$L were deposited with a syringe equipped with a 0.718 mm needle. Reported values represent the average contact angle measured after droplet deposition, once equilibrium was reached, for at least three measurements.

## 2.5 | In situ Fuel Cell Tests

### 2.5.1 | Fuel Cell Measurement Setup

Polarization curves, shown in Figures 8 and 9, were measured using a parallel graphite flow field in a single-cell setup with an active area of 5 cm$^2$. Due to commercial reasons, the details of the flow field design parameters (such as number and arrangement of flow field ribs and channels, channel pitch, and channel depth) are not disclosed here. Knowing that thermal gradients can be created between the GDL and the location of the temperature sensor, the cell temperature was monitored using a thermocouple embedded centrally within the cathode flow field plate. GDLs with 5 wt% and 20 wt% PTFE were placed onto a catalyst coated membrane (CCM) with electrode loadings of 0.38 $mg_{Pt}$ cm$^{-2}$ on the cathode and 0.10 $mg_{Pt}$ cm$^{-2}$ on the anode. The assemblies were hot-pressed to create a 5-layer Membrane Electrode Assembly (MEA). The assembled MEA was then inserted between two symmetrical flow field plates. The assembled single cell were then incorporated in a Baltic quickCONNECT fixture, ensuring gas tightness by applying a gas pressure corresponding to 1 MPa compression over the active area. The fixture was then connected to a Greenlight Innovation G60 test station equipped with a Gamry Reference 3000 potentiostat for the recording of polarization curves.

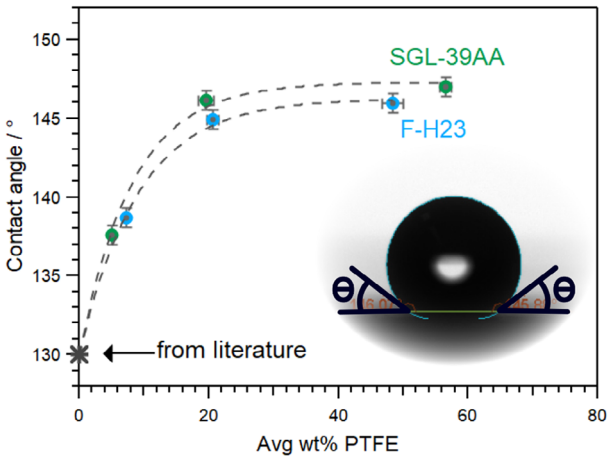


**FIGURE 2** | Contact angle values estimated using water droplets over GDL substrates subjected to the hydrophobic treatment.

### 2.5.2 | Experimental Procedure

Prior to fuel cell testing, the cell was conditioned using an internally developed protocol designed to ensure stable performance and reproducibility. The specific procedures utilized during conditioning are proprietary and cannot be disclosed here. Limiting currents were recorded by using high flow rates of $H_2$ at the anode, 0.84 NLPM, and 5.18 NLPM diluted oxygen at the cathode, for four different dry oxygen molar fractions ($\chi^{O2,dry}$). This yields high stoichiometries for all measurements, for both reactants. These testing parameters are also summarized in Table 2. Pressures are given at anode and cathode inlets, while average anode pressure drops were measured to be below 1% in all tests.

The combination of high flows and low flow field pressure gradient ($\Delta P \leq 5$ kPa) minimizes relative humidity (RH) gradients between the inlet and outlet, ensuring differential cell conditions. For each $\chi^{O2,dry}$, a polarization curve was recorded by sweeping the voltage from 0.35 V to 0.10 V, with intermediate steps of 0.05 V. Each voltage was held for 2 min, at steady-state conditions, prior to data recording. Fuel cell performance tests were designed to quantify the total resistance to gas transport ($R_{tot}$) in GDLs, based on the dry limiting current method [19]. This method is known to effectively isolate the specific contribution of GDLs and flow-field plates to oxygen transport resistance in polymer electrolyte membrane (PEM) fuel cells, allowing for an in situ evaluation of how GDL properties influence performance at limiting current conditions. Limiting currents were recorded for two different GDL microstructures, with loading of 5 wt% and 20 wt% of polytetrafluoroethylene (PTFE). The 50 wt% loading samples were not considered due to poor performance in the initial cell conditioning.

## 3 | Results and Discussion

### 3.1 | PTFE Loadings and Contact Angles

Different PTFE loadings were targeted using the hydrophobic treatment described in Figure 1, with standard deviations below 4% of the average value for F-H23 and below 6% for SGL-39AA. Further details are shown in Tables S1 and S2. Hence, the effect of this treatment on the hydrophobicity of the GDL materials was assessed by performing contact angle measurements, as described above in the Materials and Methods section. All discussed values were taken in plane, over flat GDL surfaces. Furthermore, the contact angle values for the untreated GDLs (i.e., at 0 wt% PTFE) could not be obtained due to the water droplets falling through the matrix of carbon fibers. However, for comparison a value reported in the literature for a Toray carbon paper[2] [8] with a loading of 0 wt% PTFE has been included in the plot. Figure 2 shows that the average contact angle values estimated for the two types of GDL increase steeply with PTFE loading up to around 20 wt% but only marginally beyond this value, a result that is qualitatively consistent with other findings already reported in the literature [17]. Moreover, the measured contact angle values for 20 wt% of PTFE and above are very high (~145°), indicating that both GDLs approach the superhydrophobic regime upon treatment.

### 3.2 | Raman Spectroscopy

#### 3.2.1 | Two Types of Carbon Fiber

The Raman spectra recorded from carbon fibers in the untreated GDL substrates F-H23 and SGL-39AA are shown in Figure S3 of the Supporting Information. Both spectra show the two characteristic features of carbonaceous materials, one peaked at 1315 $cm^{-1}$ in SGL-39AA and at 1342 $cm^{-1}$ in F-H23, assigned to the D mode, and another peaked at 1600 $cm^{-1}$ in SGL-39AA and at 1591 $cm^{-1}$ in F-H23, assigned to the G mode. An important difference is observed in the width of these components, being significantly narrower in the GDL SGL-39AA. For instance, the peak assigned to the D mode has a full width at half maximum (FWHM) of 118 $cm^{-1}$ in SGL-39AA but 194 $cm^{-1}$ in F-H23, as revealed by the detailed peak fitting analysis applied to these spectra. Moreover, the relatively higher intensity of the additional, low-intensity, fitting components in F-H23 (labeled 0 and 2 in Figure S4), indicates a higher degree of defects and imperfections in the carbon fibers. Altogether, these findings suggest that the carbon fibers in SGL-39AA have undergone higher graphitization temperatures during fabrication than the fibers in F-H23, resulting in higher order and fewer defects. This correlates nicely with the higher thermal conductivity values already reported for SGL materials, compared to Freudenberg GDLs [12, 20],[3] and [21].

#### 3.2.2 | Spectroscopic Signatures

Figure 3a shows the image of a spot in the GDL F-H23 with a carbon fiber covered by a white blob, later assigned to PTFE. The Raman spectra of the carbon fiber (gray trace) and the PTFE blob (blue trace) are shown in Figure 3b. This GDL had been dipped in the PTFE dispersion but was not heat treated. The blue trace reveals the characteristic spectral features of a perfluorinated carbon chain, the strongest peak at 733 $cm^{-1}$ being assigned to C-F stretching modes [22] and the one at 1380 $cm^{-1}$ to C-C stretching modes in the backbone [23]. These distinct features, in particular the integrated intensity of the isolated C-F stretching mode at 733 $cm^{-1}$, will be used to spatially locate PTFE within the GDL matrix by Raman mapping, similarly to the method used by Mendoza et al. [13].

Figure 3c shows the SEM image of a spot in the untreated SGL-39AA GDL, visualizing carbon fibers that cross each other and are held together by a binder. The spectrum of the binder (green trace) is very similar to that of the carbon fiber (gray trace), see Figure 3d, indicating that the binder consists of a carbonaceous material. Moreover, the sharp additional feature at 1582 $cm^{-1}$, along with the 2D mode at 2654 $cm^{-1}$ (Figure S5) that is not observed in the Raman spectra of the carbon fibers, indicate that the binder is substantially a graphitic material [23]. In fact, high-magnification SEM images reveal that the binder is composed of flat, micro-sized flakes (see Figure 1). Because the differences between the spectra of the binder and the carbon fiber are most evident in the D mode at ~1600 $cm^{-1}$, this has been used to spatially locate either the binder or the fiber during Raman mapping.

#### 3.2.3 | Spatial Mapping of PTFE by Raman Spectroscopy

The locations imaged by Raman spectroscopy were chosen for their proximity to notable features of the sample or extrinsic markings, in order to enable the subsequent identical location analysis by SEM and EDX. GDL samples with a PTFE loading of 20 wt% were primarily analysed, in order to match with loadings typically found in the literature [17, 24] and used in operating fuel cells. Before starting a mapping experiment, laser light of

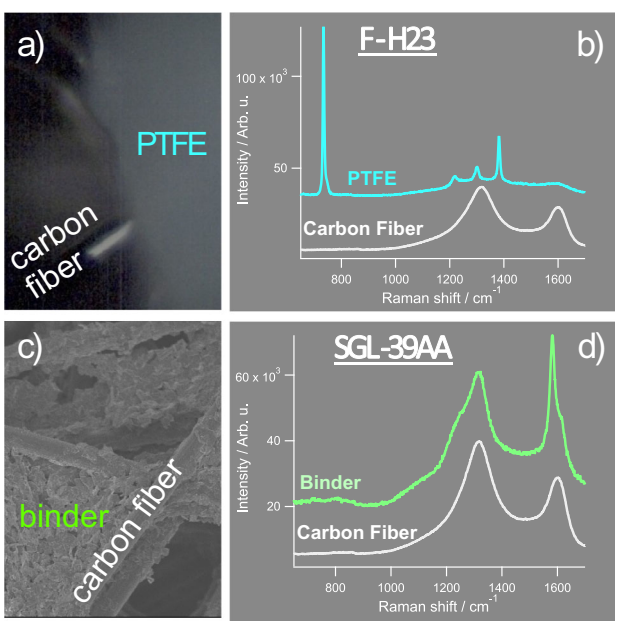


**FIGURE 3** | Raman spectra in the 650–1700 $cm^{-1}$ spectral range, recorded from the GDL substrates F-H23 (top panel) and SGL-39AA (bottom panel).

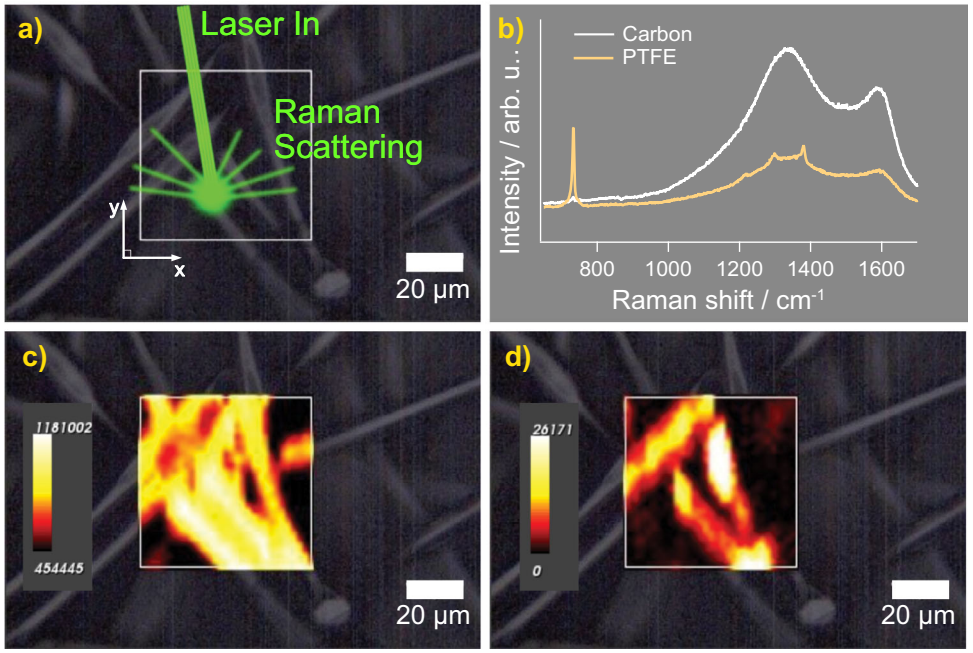


**FIGURE 4** | (a) Illustration of the Raman mapping setup for the wet-laid 20 wt% F-H23, which does not contain any preexisting binder; (b) example of a spectrum in the map from a carbon fiber (white trace) and from PTFE (yellow trace); (c) Raman map result using the area-to-baseline intensity of the D mode of the C-C bond; and (d) Raman map result using the area-to-baseline intensity of the C-F stretching mode peaked at 733 $cm^{-1}$.

low intensity was used to position the sample in the focal plane, following which a rectangular area was defined from where Raman spectra were acquired at distinct spots 2 $\mu$m apart in the $xy$ plane.[4] From these set of spectra, a heat map can be obtained based on the integrated area under selected peaks relative to a baseline. For the specific case of mapping, spectra were acquired covering the Raman shift range 620–1720 $cm^{-1}$ in the static mode.[5] The spectral window was chosen to include the characteristic signatures of both the carbonaceous domains (C-C vibrational modes) and the fluorinated compound (C-F vibrational modes).

Figure 4a shows the experimental setup used for the binder-free F-H23 GDL with 20 wt% of PTFE, set up to have the carbon fibers parallel to the $xy$ plane and the incident laser along the $z$ direction. Figure 4b shows example spectra taken from the mapping experiment in which the signature of either carbon or PTFE is very strong. Figure 4c and 4d show the Raman mapping results as heat maps using the area under the D-mode of the C-C stretching mode (c) or the area under the C-F stretching mode (d).

These mappings highlight the spatial resolution achievable by Raman spectroscopy with the setup used, around 2 $\mu m$ at the focal plane. A higher spatial resolution in $x$ and $y$ directions is possible using higher magnification objectives, but this risks rapid loss of the focal plane during measurement as well as increasing measurement time to cover the same area. A previous work using Raman spectroscopy by Mendoza et al. was focused on mapping larger areas (1000 × 1000 $\mu$m) at lower spatial resolution (10 $\mu$m) [13]. Hence, we here demonstrate the use of higher resolution Raman mapping for microstructure analysis.

Figure 4c reveals that the intensity of the C-C stretching mode reproduces very well the location of the fibers, although overlapping fibers can be hard to distinguish. In the bottom left corner of the mapped area, the lower intensity feature results from a fiber being just below the focal plane. Complementarily, the mapping results shown in Figure 4d show that the intensity of the C-F stretching mode is highest in-between the fibers, which is attributed to surface tension forces during the drying and sintering processes pulling PTFE toward the fibers. Thus, in a GDL without a preexisting binder like F-H23, the PTFE accumulates in the fiber junctions. However, we observe a lower degree of webbing between the fibers than has been reported in previous literature, either because our coating procedure involved a single, rather than multiple, dipping step or because PTFE dispersion has more fiber junctions to bind tightly to in the dense felt of the F-H23 GDL compared to other GDLs reported in the literature [11, 13, 25].

Figure 5 is organized in the same manner as Figure 4, but shows mapping results for the binder-containing GDL SGL-39AA, also with a PTFE loading of 20 wt%. The mapped area captures two straight fibers and a region in between that is rich in carbonaceous binder. An important observation is that, when detectable, the intensity of the C-F stretching mode of PTFE at 733 $cm^{-1}$ is relatively very low. In addition, a clear distinction between fiber and binder is very difficult due to the similar underlying chemistry, hence very similar Raman spectra (see Figure 4b and spectra in Figure 5b). Further, Figure 5c reveals a homogeneous presence of the binder in the whole area between the fibers. The colored intensity map of Figure 5d shows agglomerates of PTFE on the binder structure, with little or no PTFE on the carbon fibers. Hence, unlike the binder-free GDL, the PTFE preferentially deposits on the binder structure. This deposition is in the form of small agglomerates, which results in a much weaker Raman response (Figure 5b) even in areas relatively rich in PTFE. Thus, for a comparable degree

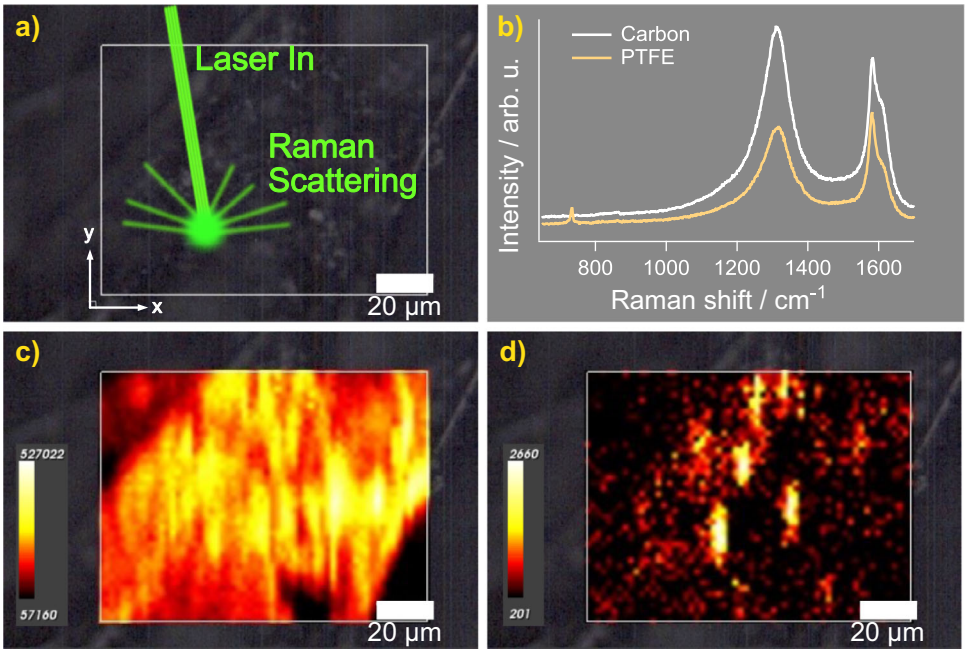


**FIGURE 5** | (a) Illustration of the Raman mapping for the dry-laid 20 wt% SGL-39AA GDL, which contains a pre-existing binder; (b) example of a spectrum in the map from a carbon fiber (white trace) and from the binder phase (yellow trace); (c) Raman map result using the area-to-baseline intensity of the D mode of the C-C bond; and (d) Raman map result using the area-to-baseline intensity of the C-F stretching mode peaked at 733 $cm^{-1}$.

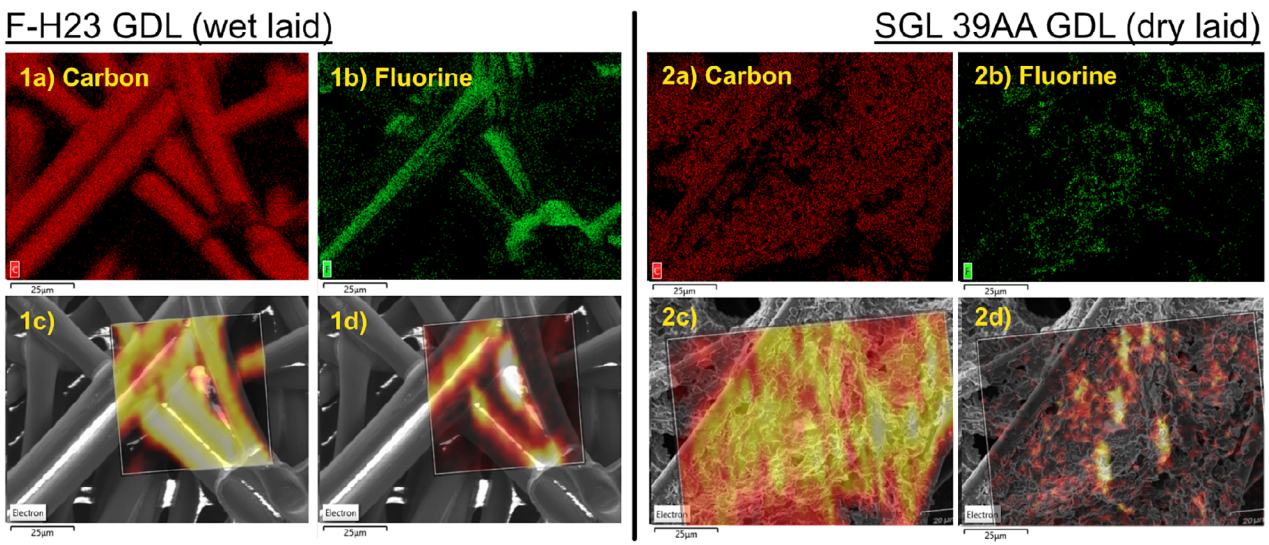


**FIGURE 6** | EDX images (top row) of the same areas mapped with Raman in Figure 4 and Figure 5 (bottom row). Left: F-H23 GDL; EDX maps of Carbon (1a) and Fluorine (1b), alongside previously recorded Raman maps of the C-C bond (1c) and C-F bond (1d) overlaid onto the SEM image from Figure 1. Right: SGL-39AA; EDX maps of Carbon (2a) and Fluorine (2b), alongside previously recorded Raman maps of the C-C bond (2c) and C-F bond (2d) overlaid onto the SEM image from Figure 1.

of hydrophobization, the local density of PTFE at detected spots is much lower in SGL-39AA than in F-H23. Altogether, these observations let us conclude that in SGL-39AA, PTFE finds the native binder as a scaffold for binding, leading to a more dispersed polymer and locally weaker Raman intensities. Differently from the case of F-H23, in SGL-39AA PTFE remains disconnected from the fiber junctions, as will be confirmed later by EDX analysis performed at identical locations (Figure 6).

### 3.3 | SEM and EDX Analysis

SEM was used to gain higher resolution images of the GDL microstructure, while EDX was used to complement the Raman mapping by tracking the signal of fluorine through space. Notably, the imaged areas in Figure 6 are identical to those mapped in Figure 4 and Figure 5, and shown in Figure 1. The Supporting Information file contains a repeat of this experiment in Figure S6.

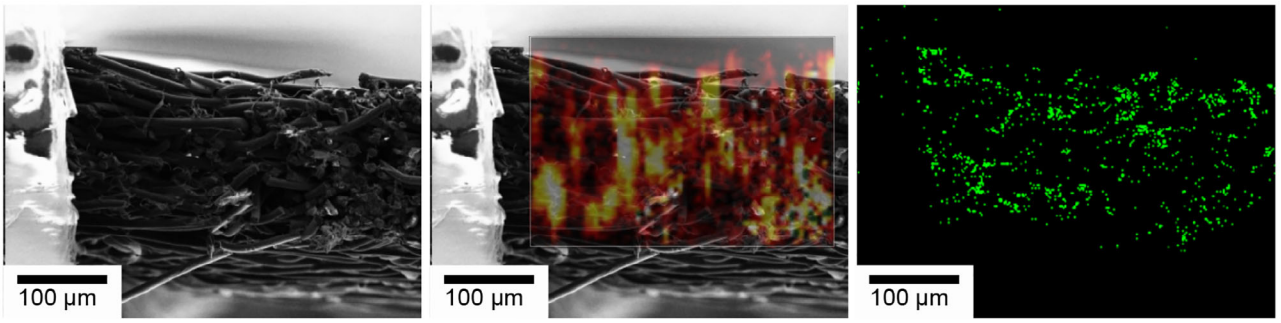


**FIGURE 7** | SEM image of a cryocut cross section of the binder-free F-H23 GDL with 20 wt% PTFE loading (left), Raman mapping of the cross section overlaid onto the SEM image (center), and the EDX map for fluorine of the same area (right). The Raman mapping is created from the same C-F stretching signal presented previously.

The microstructure of the binder-free, wet-laid F-H23 GDL (Figure 6, left) consists of bended fibers that overlap strongly, with the PTFE polymer accumulating primarily where the fibers intersect. In both EDX and Raman mappings, the fluorine is visible in between the carbon fibers. These gaps between the fibers represent a relatively small portion of the whole gas-accessible volume of the GDL, pointing to hypothetically limited losses of the mass transport properties (further discussed below). The EDX signals from fluorine and carbon are very distinct and enable an easy discrimination of the compound that they belong to. Nevertheless, EDX mapping is limited by the loss of signal from deep parts of the samples and from orientations facing away from the EDX detector. Interestingly, the carbon EDX map and the C-C bond Raman map overlap very nicely over the probed fibers. Similarly, the fluorine EDX map and the Raman map of the C-F bond observe the same clusters of PTFE in the binder-free GDL.

The binder-containing dry-laid SGL-39AA GDL (Figure 6, right) consists of thinner, more straight fibers with a native carbonaceous binder that is relatively difficult to distinguish from the fibers in both Raman and EDX. The fluorine EDX signal and the C-F bond Raman signal are both significantly weaker compared to the case of F-H23 GDL. Thus, the EDX map confirms the result from Raman mapping that fluorine is spatially very dispersed over the surface area of the binder. This is because the electron beam, even at a low acceleration voltage of 5 kV, has a very large interaction volume in the less dense binder phase, which results in each point containing some fluorine signal from neighboring regions. Both methods converge in telling that PTFE is more dispersed and broadly distributed within the binder phase in SGL-39AA (evidenced particularly clearly by Raman spectroscoopy), while it is found primarily along the fibers and at intersection points in F-H23.

### 3.4 | Cross-Sectional Mapping

Figure 7 shows the results from a cross-sectional analysis of a binder-free F-H23 GDL with 20 wt% PTFE, which had been cryo-cut in liquid nitrogen. The 20 wt% PTFE loading matches that used in other studies while the absence of the binder results in stronger signals from PTFE.[6] The probed area spans the entire thickness of the GDL, which is about 200 $\mu$m. The carbon fibers are primarily flat over the $xy$ plane but otherwise randomly oriented, whereby the analyzed cross-sectional area exposes both entire fibers and their cut cross-sections, including large empty areas between the fibers themselves. In these morphological conditions,[7] and while covering large areas, the focal plane is easily lost and it was necessary to use a lower magnification objective. In our case, a 20× ($NA$ = 0.4) Leica objective was used whereby the distance between collection points was adjusted to 5 $\mu$m. We emphasize that while some studies exist on the inhomogeneous properties of GDLs through-plane by 2D surface mapping [10], cross-sectional investigations remain rare, particularly using Raman spectroscopy.

On this line, EDX has been used to analyze cross-sections of GDLs [11, 14] but, to the best of our knowledge, Raman spectroscopy has yet not been used to obtain cross-sectional maps. In a previous work [13], Raman spectra were acquired in-depth varying the focal plane to penetrate the fiber matrix from above, although this method suffers from lost confocality upon penetration and undesired, obstructing features along the path of the laser. Here, by 2D mapping a full cross-sectional area with confocal Raman spectroscopy, we demonstrate that it is possible to gain detailed information about the distribution of PTFE across the whole thickness of a GDL. By contrast, the cross sections of the GDL SGL-39AA were extremely challenging to analyze, due to the extremely high porosity and to the PTFE primarily laying along in-plane layers of the GDL.

The results shown in Figure 7 reveal that the GDL is fully penetrated by PTFE, which is present in the form of agglomerates that are independent of depth within the GDL. Analysis of these results is tricky; in the Raman map, regions further in the GDL that are outside the focal plane contribute to the overall signal but are not in focus and so contribute a lower amount than regions that are at focus. Meanwhile in the EDX map, the focused electron beam makes these focus artifacts less relevant, however the resulting $X$-rays from further in the sample are more likely to be blocked by parts of the GDL before they can reach the detector, leading to a similar effect. What is nonetheless clear is that the distribution of PTFE is not depth dependent in the analyzed sample, hence results taken from regions relatively close to the GDL surface should be representative of the interior parts as well. Further cross-section data are shown in Figures S7 and S8.

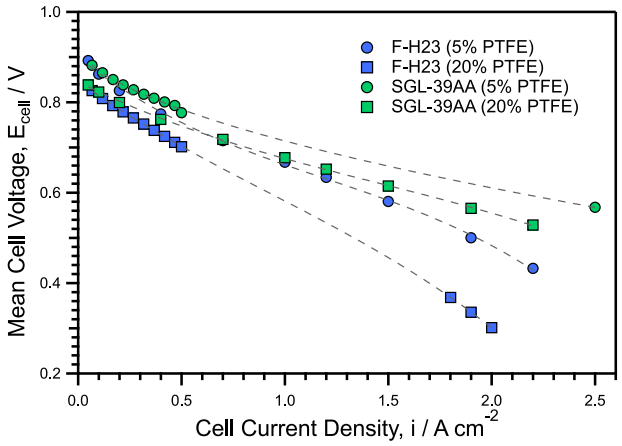


**FIGURE 8** | $H_2$/air polarization curves recorded during fuel cell operation using MEAs assembled with the different GDL materials.

In previous studies, Fishman and Bazylak used CT [10] to show major discrepancies in the PTFE distribution depending on the drying method applied to similar Toray GDL materials; air dried samples showing high concentrations of PTFE at the outer surfaces of the GDL. Ito et al. [11] saw PTFE distributions that were independent of depth only in the case of vacuum drying, attributed to the lack of capillary forces on the PTFE dispersion. Despite also using an air-drying method, the results presented in our work show agglomerations that form at every depth in the GDL with little difference near the outer surface. We attribute this to the initial drying step on absorbent paper which removes excess dispersion from the GDL.

From the distribution of PTFE shown in Figures 4–7, we propose the following mechanism. Considering that PTFE is initially applied as an aqueous dispersion that is subsequently dried, we suppose that PTFE preferentially deposits at the sites where it can maximize contact to the carbonaceous support, as even with low wettability some adhesion force remains. The fibers and binders considered here are carbonaceous (albeit with different degrees of graphitization) and very weakly hydrophilic [26]. This may lead to droplets with dispersed PTFE favoring spots with a high surface area, such as the junctions between fibers in the case of F-H23, or the platelet structures on the binder in the case of SGL-39AA. During drying, such droplets shrink, concentrating their PTFE and forming agglomerates.

We note that the two GDLs studied here differ not only in the presence of a native binder, but also in fiber morphology, degree of graphitization, porosity, and thickness. While we propose the binder as the primary driver of the observed differences in PTFE distribution, contributions from these other structural differences cannot be excluded. A definitive isolation of the binder effect would require a controlled comparison using GDL substrates that are identical in all properties except for the presence of the binder, which we identify as an important direction for future work.

### 3.5 | In Situ Fuel Cell Performance

In the full polarization curves reported in Figure 8, the three different regions reflecting losses due to activation, ohmic resistance, and mass transport can be distinguished. At low current densities, the observed differences are within the range of MEA-to-MEA variability. Comparison of GDL/PTFE combinations is instead made in the region of mass transport losses, which is supported by the limiting current density measurements discussed below.

Dry limiting current tests were performed to quantify the resistance to oxygen transport under dry conditions. This method, as described by Baker et al. [19], involves operating the PEM fuel cell at low oxygen concentrations while gradually decreasing the cell voltage until a limiting current is observed, that indicates oxygen starvation in the catalyst layer. In the limiting current density regime, only the structural properties (i.e., porosity and tortuosity) of the material are expected to contribute to the local transport of oxygen. The test is repeated at multiple total pressures. Under differential flow conditions and using a small active area, the system maintains a uniform inlet gas composition and the total oxygen transport resistance, $R_{tot}$, can be obtained as [19, 27, 28]:

$$R_{tot}^{O_2,dry} = \frac{4 \cdot \mathcal{F} \cdot \chi^{O_2,dry}}{i_{lim}} \cdot \frac{p - p_w}{\mathcal{R} \cdot T}, \quad (1)$$

where $\mathcal{F}$ is the Faraday's constant, $\chi^{O_2,dry}$ is the dry inlet oxygen mole fraction, $p$ is the absolute pressure, $p_w$ is the partial pressure of water vapor (calculated as 23.1 kPa from the RH and the Antoine equation), $i_{lim}$ is the limiting current, $\mathcal{R}$ is the ideal gas constant, and $T$ is the temperature [19, 28, 29].

The limiting current measurements presented in Figure 9 were obtained at an absolute inlet pressure of 150 kPa across four dry oxygen molar fractions, for both GDL types under the operating conditions summarized in Table 2 (see additional data in Figure S9). Excluded from this are the GDLs with 50 wt% of PTFE due to their poor performance during the conditioning phase, hypothesized to be due to excessive ohmic losses. The limiting current was extracted from each polarization curve as the current density recorded at a cell voltage of 0.15 V. At oxygen concentrations of 0.5%, 1%, and 2%, the polarization curves became nearly vertical before this voltage threshold, confirming that mass-transport limitation was fully established and that the measured current closely approximates the true limiting current. At 4% $O_2$, however, the curves did not reach verticality, indicating that contributions from kinetic and ohmic losses remained significant at higher current densities. Consistently with this observation, Figure 10a shows that the limiting current at 4% oxygen deviates a bit from the otherwise linear dependence on oxygen mole fraction seen at lower concentrations (see also Figure S10 for data at other pressures). Consequently, the transport resistance values derived at 4% $O_2$ carry greater uncertainty and should be interpreted with caution.

The total dry oxygen transport resistances were calculated from Equation (1), whereby each $R_{tot}$ was separated into a pressure dependent ($R_P$) and a pressure independent ($R_{NP}$) part (see also Figure S11 and Table S3 for the obtained values). In this decomposition, $R_P$ represents the molecular gas phase transport resistance, primarily governed by transport through the macroporous GDL substrate, while $R_{NP}$ captures transport losses within the catalyst layer arising from Knudsen diffusion in the gas phase

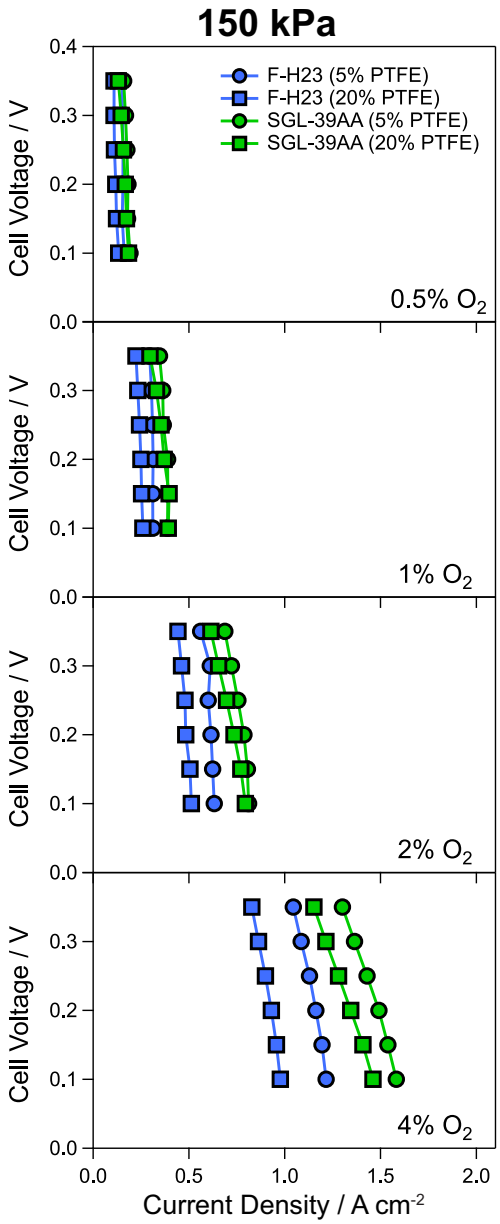


**FIGURE 9** | Limiting current density vs cell voltage for the two GDL materials (both with 5% and 20% PTFE loading) at different oxygen mole fractions, all shown for the case of 150 kPa of absolute pressure. Corresponding data for 200 kPa and 300 kPa of absolute inlet pressure are shown in Figure S9.

and from oxygen transport through the ionomer films. The $R_P$ values reported in Figure 10b are systematically lower for the binder-containing SGL-39AA GDL than for the binder-free F-H23 GDL, an observation that is confirmed true for all inlet absolute pressures (Figure S11). This trend is consistent with the earlier onset of mass transport limitations observed in the corresponding polarization curves shown in Figure 8.

We see from Figures 10b and S11 that $R_P$ is influenced more heavily by the type of GDL than the amount of PTFE, at all experimental conditions. This demonstrates the importance of the underlying microstructure for the resistance to oxygen transport, with the binder-containing GDL studied here having lower $R_P$ values on account of its higher effective porosity. We note, however, that the lower $R_P$ values observed for SGL-39AA compared to F-H23 cannot be attributed solely to the presence of the native binder, as these two commercial GDLs also differ in fiber morphology, porosity, and thickness. The observed differences in oxygen transport resistance should therefore be interpreted as reflecting the overall microstructural differences between the two materials, of which the binder is one contributing factor.

Further, while $R_P$ is clearly dominated by the underlying GDL microstructure, the pressure-independent component $R_{NP}$ captures transport losses associated with Knudsen diffusion and oxygen permeation through ionomer films in the catalyst layer. It is plausible that differences in PTFE distribution between the two GDL types influence how uniformly the ionomer is covered at the GDL/catalyst layer interface. In the binder-containing SGL-39AA, where PTFE is dispersed broadly over the binder phase, the interface presented to the catalyst layer may be more homogeneous than in F-H23, where PTFE agglomerates are concentrated at fiber junctions. Establishing whether this structural difference translates into measurable differences in $R_{NP}$ would require a dedicated investigation of the catalyst layer interface, which is beyond the scope of the present work but represents a relevant direction for future study.

As we have shown in Figures 4, 5, and 6, PTFE preferentially deposits over the binder when it is present and in fiber junctions when it is not. It appears that for the binder-containing SGL-39AA GDL, PTFE is contributing little to $R_P$ because it is depositing in areas already sealed by the preexisting binder. In the binder-free F-H23 GDL it deposits in fiber junctions, with the potential to increase $R_P$. However, we do not observe such an increase, suggesting that the blocked volume is insufficient to qualitatively alter the available pore volume. While literature on oxygen transport resistance in the case of a preexisting binder is sparse, it is expected that $R_P$ is substantially controlled by the GDL microstructure. These results also suggest that the effect of PTFE becomes more relevant under wet, or humid operating conditions [17, 24, 29].

In terms of GDL design, these findings indicate that binder-containing GDLs may have more freedom to use higher quantities of hydrophobic polymers, which may allow for the easier adoption of non-PFSA materials. Further, as the binder phase appears to be the preferential location for PTFE deposition, it could be utilized to control the PTFE distribution within a GDL. We stress that different fiber/binder combinations may exhibit different behavior if made of dissimilar materials to the F-H23 and SGL-39AA studied here. Demonstrating such an effect is, however, beyond the scope of this article and may instead be the focus of a follow-up study.

## 4 | Conclusions

In this article, we have investigated how the distribution of PTFE, introduced by a dip-coating and sintering method, varies across the case of two types of GDL, which differ in the presence of a preexisting carbonaceous binder as well as in

**TABLE 2** | Operating conditions for in situ fuel cell testing.

| Parameter | Anode | Cathode |
|---|---|---|
| Flow rate | 0.84 NLPM | 5.18 NLPM |
| Absolute inlet pressure | 150, 200, 300 kPa | 150, 200, 300 kPa |
| Fuel humidification | 60% RH | 60% RH |
| Fuel concentration | 100% ($H_2$) | 0.5%, 1%, 2%, 4% ($O_2$) |
| Temperature at inlet | 75°C | 75°C |
| Coolant flow rate | 0.5 NLPM | |
| Coolant temperature (inlet) | 70°C | |

Abbreviation: NLPM, normal liters per minute.

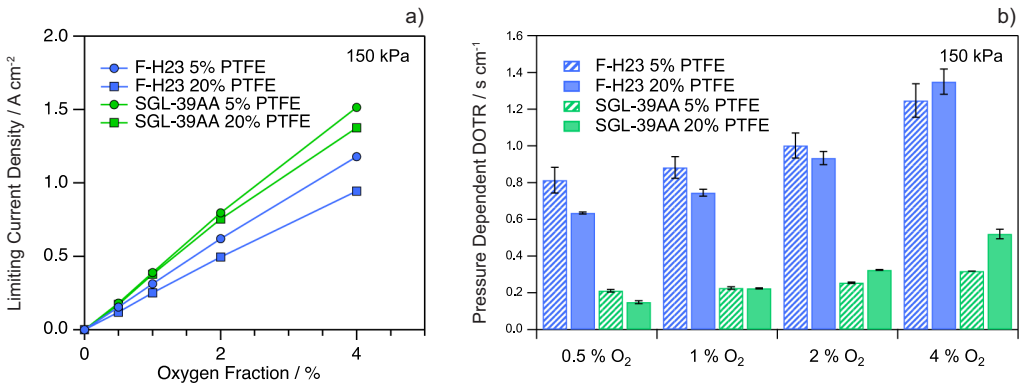


**FIGURE 10** | Limiting current density versus mole fraction of oxygen (a) and bar plot of the pressure dependent portion of the total dry oxygen transport resistance (DOTR), (b) for the two GDL materials (with 5% and 20% PTFE loading), at an absolute pressure of 150 kPa. Corresponding data for 200 kPa and 300 kPa of total pressure are shown in Figures S10 and S11.

porosity and fiber morphology. Moreover, we present an original method investigating identical locations in each GDL material by both confocal Raman and SEM-EDX mapping, as well as we show the first case of an identical location analysis by both Raman and SEM-EDX of a full-width cross-sectional GDL area, 200 × 300 μm wide.

We find that in the binder-free, wet-laid F-H23 GDL the PTFE accumulates preferentially at the junctions between the fibers and over the fibers' surface, while for the dry-laid SGL-39AA GDL that contains a pre-existing binder, the PTFE forms less dense agglomerates primarily over the binder phase. This is visible in both Raman and SEM-EDX mapping. Analysis of the cross section of the binder-free F-H23 GDL shows that the PTFE agglomerates formed through the thickness of the sample are stochastically distributed through thickness rather than weighted toward one side of the GDL. We emphasize that the findings reported here are specific to the F-H23 and SGL-39AA commercial GDLs studied, and should not be generalized as a universal mechanism governing all binder-containing GDL systems. We identify a rigorous isolation of the binder effect as a priority for future work.

Although the present study focused exclusively on dry gas transport conditions, the observed differences in PTFE distribution offer a basis for anticipating the behavior of the two GDL types under humid or wet operating conditions. In the binder-free F-H23 GDL, PTFE concentrated at fiber junctions may provide effective local barriers against liquid water ingress at those specific sites, but leaves the remainder of the pore space relatively unprotected. By contrast, the broader distribution of PTFE across the binder phase in SGL-39AA may result in a more uniform hydrophobic coverage of the internal pore surfaces, potentially offering more consistent resistance to flooding. On this basis, we tentatively suggest that SGL-39AA may exhibit more stable water management under high-humidity conditions, though this hypothesis requires experimental validation, which we identify as a priority for a follow-up work.

Finally, we emphasize that in a future scenario where an organic, non-fluorinated compound may serve as the hydrophobic ingredient, SEM-EDX alone will not be sufficient to spatially resolve it from the carbonaceous fiber; while confocal Raman spectroscopy may, depending on the chosen polymer's chemistry, be able to make a distinction through the specific signatures of vibrational modes in each component.

### Author Contributions

**Dylan Schulz:** Methodology, Investigation, Visualization, Writing – Original Draft. **Marcus Ringström:** Conceptualization, Investigation, Formal Analysis, Writing – Original Draft. **Siva Ravi Sankar:** Investiga-

tion, Methodology. **Anna Martinelli:** Supervision, Resources, Writing – Review & Editing.


### Acknowledgments

The authors acknowledge Kalle Genheden at PowerCell Sweden AB for conducting the in situ fuel cell tests. The authors also thank Stefan Gustafsson and the Chalmers Materials Analysis Laboratory (CMAL) as well as Sasha Vuckovic and Spectral AB for the use of SEM and EDX instruments. Romain Bordes at Chalmers University of Technology is acknowledged for his assistance with contact angle measurements, and Dhanya Raghunathan for advice and fruitful discussions. In part, this project is financed through the Swedish Electricity Storage and Balancing Centre (SESBC). The Centre is funded by the Swedish Energy Agency together with five academic and 28 non-academic partners. In particular, the authors acknowledge VGR, Smoltek, Celcibus, Hymeth, Ionautics, Nilsson Energy, Hitachi Energy, SvK, and Nanoscientifica for their contribution and support to the project. The authors would like to thank the Swedish Energy Agency also via the Swedish Electromobility Center (SEC) and the Swedish governmental initiative StandUp for Energy are kindly acknowledged.


### Disclosure

During the preparation of this work, the authors used Google Gemini in order to review drafts and provide feedback. AI was not used to generate any content. After using Gemini, the authors reviewed and edited the content as needed and take full responsibility for the content of the published article.

### Conflicts of Interest

The authors declare no conflicts of interest.

### Data Availability Statement

Data are available from the authors upon request.

### Endnotes

The actual PTFE loading values did not always perfectly correspond to the target values; further details are given in Tables S1 and S2. Moreover, the 50 wt% targeted GDL samples were excluded from in situ data analysis, due to their poor performance during fuel cell conditioning (see Sections 2.5.2 and 3.5).

A TGP-060, 190 $\mu$m in thickness and 76% porosity.

In this reference, the thermal conductivity with MPL coating was measured for a Freudenberg H15C14 and an SGL 22BB. Although not identical, these are materials very similar to the materials studied in this work, and can therefore serve as a useful reference.

The $z$ direction being parallel to the direction of propagation of the incident laser.

In the static mode of collection, a fixed spectral window approximately 1200 $cm^{-1}$ wide is detected, allowing fast spectral acquisitions.

The binder-containing SGL-39AA GDL featured already lower intensity signals and greater challenges focusing on the sample, since the dominant orientation of fiber and binder species is within the $xy$ plane. This lead to very poor signal to noise ratios during cross section mapping attempts.

The porous and tortuous character of the cross-sectional areas, which contain round-shaped fibers, does not provide flat surfaces which would be ideal for 2D mapping; many collection spots fall above or below the focal plane and therefore loose resolution. This morphology causes issues also during EDX analysis, mainly related to shadowing effects.

### References


1. European Commission, A Hydrogen Strategy for a Climate-Neutral Europe, Tech. Rep. COM(2020) 301 final, (European Commission, Brussels, 2020).

2. BloombergNEF, *Hydrogen Economy Outlook: Key Messages* (BloombergNEF, March 2020).

3. M. Mathias, J. Roth, J. Fleming, and W. Lehnert, "Diffusion Media Materials and Characterisation," in *Handbook of Fuel Cells*, Vol. 3 (John Wiley and Sons, 2010), 20–22.

4. R. Flückiger, S. A. Freunberger, D. Kramer, A. Wokaun, G. G. Scherer, and F. N. Büchi, "Anisotropic, Effective Diffusivity of Porous Gas Diffusion Layer Materials for PEFC," *Electrochimica Acta* 54, no. 2 (2008): 551–559.

5. W.-M. Yan, C.-Y. Hsueh, C.-Y. Soong, F. Chen, C.-H. Cheng, and S.-C. Mei, "Effects of Fabrication Processes and Material Parameters of GDL on Cell Performance of PEM Fuel Cell," *International Journal of Hydrogen Energy* 32 (2007): 4452–4458.

6. T. Chen, S. Liu, J. Zhang, and M. Tang, "Study on the Characteristics of GDL With Different PTFE Content and Its Effect on the Performance of PEMFC," *International Journal of Heat and Mass Transfer* 128 (2019): 1168–1174.

7. K. Zhou, T. Li, Y. Han, J. Wang, J. Chen, and K. Wang, "Optimizing the Hydrophobicity of GDL to Improve the Fuel Cell Performance," *RSC Advances* 11, no. 4 (2021): 2010–2019.

8. M. Mortazavi and K. Tajiri, "Effect of the PTFE Content in the Gas Diffusion Layer on Water Transport in Polymer Electrolyte Fuel Cells (PEFCs)," *Journal of Power Sources* 245 (2014): 236–244.

9. G.-G. Park, Y.-J. Sohn, T.-H. Yang, Y.-G. Yoon, W.-Y. Lee, and C.-S. Kim, "Effect of PTFE Contents in the Gas Diffusion Media on the Performance of PEMFC," *Journal of Power Sources* 131, no. 1-2 (2004): 182–187.

10. Z. Fishman and A. Bazylak, "Heterogeneous Through-Plane Porosity Distributions for Treated PEMFC GDLs. I. PTFE Effect," *Journal of the Electrochemical Society* 158, no. 8 (2011): B841.

11. H. Ito, K. Abe, M. Ishida, et al., "Effect of Through-Plane Distribution of Polytetrafluoroethylene in Carbon Paper on In-Plane Gas Permeability," *Journal of Power Sources* 248 (2014): 822–830.

12. H. Sadeghifar, N. Djilali, and M. Bahrami, "Effect of Polytetrafluoroethylene (PTFE) and Micro Porous Layer (MPL) on Thermal Conductivity of Fuel Cell Gas Diffusion Layers: Modeling and Experiments," *Journal of Power Sources* 248 (2014): 632–641.

13. A. Mendoza, M. Hickner, J. Morgan, K. Rutter, and C. Legzdins, "Raman Spectroscopic Mapping of the Carbon and PTFE Distribution in Gas Diffusion Layers," *Fuel Cells* 11, no. 2 (2011): 248–254.

14. A. Rofaiel, J. Ellis, P. Challa, and A. Bazylak, "Heterogeneous Through-Plane Distributions of Polytetrafluoroethylene in Polymer Electrolyte Membrane Fuel Cell Gas Diffusion Layers," *Journal of Power Sources* 201 (2012): 219–225.

15. X. Zhuo, S. Sui, and J. Zhang, "Electrode Structure Optimization Combined With Water Feeding Modes for Bi-Functional Unitized Regenerative Fuel Cells," *International Journal of Hydrogen Energy* 38, no. 11 (2013): 4792–4797.

16. A. Kakaee, G. Molaeimanesh, and M. E. Garmaroudi, "Impact of PTFE Distribution Across the GDL on the Water Droplet Removal From a PEM Fuel Cell Clectrode Containing Binder," *International Journal of Hydrogen Energy* 43 (2018): 15481–15491.

17. C. Lim and C. Wang, "Effects of Hydrophobic Polymer Content in GDL on Power Performance of a PEM Fuel Cell," *Electrochimica Acta* 49, no. 24 (2004): 4149–4156.

18. C. Patrick, "Thermal Stability of Polytetrafluoroethylene," *Nature* 181, no. 4610 (1958): 698–698.

19. D. R. Baker, C. Wieser, K. C. Neyerlin, and M. W. Murphy, "The Use of Limiting Current to Determine Transport Resistance in PEM Fuel Cells," *ECS Transactions* 3, no. 1 (2006): 989.

20. V. Leduc, G. Sdanghi, R. Bligny, et al., "A Practical Method for the In Situ Estimation of the Effective Thermal Resistance of Gas Diffusion Layers in PEMFC," *Electrochimica Acta* 505 (2024): 145001.

21. R. Bock, A. D. Shum, X. Xiao, et al., "Thermal Conductivity and Compaction of GDL-MPL Interfacial Composite Material," *Journal of the Electrochemical Society* 165, no. 7 (2018): F514–F525.

22. J. Koenig and F. Boerio, "Raman Scattering and Band Assignments in Polytetrafluoroethylene," *Journal of Chemical Physics* 50, no. 7 (1969): 2823–2829.

23. Y. Wang, D. C. Alsmeyer, and R. L. McCreery, "Raman Spectroscopy of Carbon Materials: Structural Basis of Observed Spectra," *Chemistry of Materials* 2, no. 5 (1990): 557–563.

24. Y. Chen, T. Tian, Z. Wan, F. Wu, J. Tan, and M. Pan, "Influence of PTFE on Water Transport in Gas Diffusion Layer of Polymer Electrolyte Membrane Fuel Cell," *International Journal of Electrochemical Science* 13, no. 4 (2018): 3827–3842.

25. H. Ito, K. Abe, M. Ishida, C. M. Hwang, and A. Nakano, "Effect of Through-Plane Polytetrafluoroethylene Distribution in a Gas Diffusion Layer on a Polymer Electrolyte Unitized Reversible Fuel Cell," *International Journal of Hydrogen Energy* 40, no. 46 (2015): 16556–16565.

26. B. Ramos-Alvarado, "Water Wettability of Graphene and Graphite, Optimization of Solid-Liquid Interaction Force Fields, and Insights From Mean-Field Modeling," *Journal of Chemical Physics* 151, no. 11 (2019): 114701, https://doi.org/10.1063/1.5118888.

27. C. Simon, F. Hasché, D. Müller, and H. A. Gasteiger, "Influence of the Gas Diffusion Layer Compression on the Oxygen Mass Transport in PEM Fuel Cells," *ECS Transactions* 69 (2015): 1293–1302.

28. M. A. Rahman, et al., Electrochimica Acta 320 (2019): 1–12.

29. D. R. Baker, D. A. Caulk, K. C. Neyerlin, and M. W. Murphy, "Measurement of Oxygen Transport Resistance in PEM Fuel Cells by Limiting Current Methods," *Journal of The Electrochemical Society* 156 (2009): B991.

## Supporting Information

Additional supporting information can be found online in the Supporting Information section.

**Supporting File:** fuce70139-sup-0001-SuppMat.pdf.